A novel magnetic transmission for powerful miniature surgical robots

Mihai Nica, Cameron Forbrigger, *Student Member, IEEE,* and Eric Diller, *Member, IEEE,*

***Abstract*—Untethered magnetically actuated robots present significant advantages for biomedical applications by allowing power to be delivered wirelessly to remote, miniature robots through flesh and bone. Nevertheless, generating enough usable force to interact with their environment remains a challenge: most millimeter-size magnetic robots achieve forces of much less than 0.1 N, which limits their medical applications. Therefore, a compact, millimeter-scale transmission is needed to amplify the output force. A novel micro-transmission system is presented, composed of a driving magnet suspended between two twisted string actuators. An analytical model of the transmission is formulated to predict its behavior under both fixed load and fixed displacement configurations. Experimental measurements are used to validate the predicted maximum achievable force, to quantify the transmission performance over numerous cycles, to determine the effect of different string materials, and to determine the impact of hysteresis and viscoelasticity. Finally, the transmission is integrated into a 3 mm diameter surgical gripper prototype to demonstrate its effectiveness. With only a modest 20 mT of applied magnetic field, the gripper generates 1.09 N gripping force - a factor of 35 improvement in mechanical advantage and a factor of 62 improvement in gripping force compared to a similar size gripper using direct magnetic actuation. This micro-transmission for miniature magnetic robots will enable high-strength untethered robots for minimally invasive surgical applications.**

***Index Terms*—Actuators and sensors; robotics: mechanisms, design, modelling & control; medical robotics.**

I. Introduction

MAGNETIC actuation is being increasingly used for wireless actuation medical robots. With external sources of magnetic field, such as electromagnetic coils or banks of permanent magnets, high-speed forces and torques can be transmitted safely and wirelessly to miniature magnetic end-effectors through tissue and bone [1]. As a result of their scalability, biocompatibility, and versitility, untethered miniature magnetic robots are being developed to replace painful biopsies, drug deliveries, and open surgical interventions with minimally-invasive surgical (MIS) robotic procedures [2]. Compared with cable- or motor-driven medical robots, wireless magnetic actuation shows promise for smaller and less-invasive end effectors to advance MIS.

One area that would benefit immensely from powerful untethered tools is neurosurgery. A survey among neurosurgeons concluded that a lack of high-strength, dexterous, miniature tools is a key barrier to advancement in MIS [3]. The ideal tools would be smaller than 3 mm across in the closed configuration, to fit through a thin trocar into the brain, while exerting median forces on the order of 100 mN for tissue cutting and retraction [4].

Currently, many magnetic robots at the required millimeter scale, such as grippers [5]–[7], microrobots moving through fluids [8]–[11] and others [12]–[14] achieve usable forces 1-2 orders of magnitude less than that required for surgical tasks (see Fig. S1 in the Supplementary Materials). Indeed, compared to other microactuation methods, such as electric field propulsion, piezoelectric actuation, light, acoustic, and thermal actuation, magnetic actuation typically achieves less effective force [15]–[22]. In existing magnetic robots, magnetic forces and torques are applied directly to embedded magnets within the simple microrobot body. These forces scale with the volume of the magnets on-board the end effector; thus, output forces are highly scale-dependent. While the actuation force of these magnetic systems can be increased by applying larger magnetic fields using enormous electromagnets [23], gains diminish as electromagnet size increases.

Consequently, a miniature transmission is needed that can amplify the output force of magnetically actuated milli-robotic devices. Such a transmission must be mechanically simple to allow for miniaturization to millimeter or smaller scales while remaining reliable and robust. Conventional mechanical transmissions involving multiple parts, such as gear trains, are inherently challenging to build at the sub-millimeter scale, due to tight fabrication and assembly tolerances [24], and difficult to operate smoothly due to friction and adhesion forces outweighing inertia at such small sizes [12]. In contrast, the twisted string actuator (TSA) is a transmission mechanism which converts high-speed, low-torque input into a low-speed, high-force output through a very simple principle: as a string or bundle of strings is twisted, its length shortens, as depicted in Fig. 1-(B). Previous research studied the kinematics of the TSA actuated with electric motors [25]–[27] and concluded that they excel at amplifying force at scales of 40-70 cm. In addition, the TSA has potential for capabilities such as self-sensing of deformation [28]. However, miniaturizing the conventional TSA is challenging because it needs a power source, often a DC motor. Additionally, long twisted strings can pose operational and friction problems, especially if the strings pass around corners or through conduits [29]. Combining magnetic actuation with twisted string actuators can overcome these challenges by allowing wireless power transmission directly to the tool while maintaining high output forces.

This work was supported in part by the Natural Sciences and Engineering Research Council of Canada through the Discovery Grant Program 2014-04703 and in part by the Canadian Institutes of Health Research under Grant CPG-158271. (*Corresponding author: Eric D. Diller.*)

M. Nica, C. Forbrigger, and E. Diller are with the Department of Mechanical and Industrial Engineering, University of Toronto, 5 King's College Rd, Toronto, ON M5S 3G8 ediller@mie.utoronto.ca

We propose, for the first time, a magnetically-actuated TSA, where an externally-applied magnetic field will be used to rotate a small magnet attached directly to the TSA as depicted in Fig. 1. The entire magnetic TSA assembly can be embedded in the application workspace with short and thin strings, and its completely wireless actuation capabilities will enable future untethered robot designs. On the other hand, wireless actuation will also leave more room in tethered designs for other critical surgical robot systems, such as signal lines for vision and contact sensors.

The main objective of this study is to introduce a novel miniature magnetic TSA that can be remotely operated with magnetic fields to achieve high actuation forces of more than 1 N, or 10 times the force required for typical tissue retraction of 100 mN. By aiming at producing a high force output, more design flexibility is achieved by allowing the possibility of integrating this transmission in a microrobotic environment. A mathematical model that predicts the maximum achievable force of the TSA under various operating conditions was derived and evaluated experimentally. This model is novel in that it develops expressions for both the force and torque in a TSA after an initial twist, where the string shortens to an axial blocking point and subsequently keeps twisting to develop an axial force. The model allows us to explore the design space to show the potential of this concept in this and other applications. To illustrate the application of this transmission for microsurgery, a miniature (3 mm diameter) surgical gripper prototype is introduced. The tool uses a magnetically-actuated TSA that can produce gripping forces of greater than 1 N: a factor of 62 increase compared to a gripper actuated by direct magnetic actuation with the same magnetic volume [5], which opens many possibilities for miniaturizing existing robotic surgical tools while still achieving high forces.

This manuscript is divided into three main sections. In the first section, an analytical model is introduced that predicts the force output of a TSA as a function of the rotation angle. A dimensional analysis is performed to define characteristic parameters that determine the performance of a given TSA design. In the next section, a series of experiments are conducted to validate the analytical model for a variety of string materials and geometries and the results of these experiments are discussed. This discussion leads to the formulation of a set of design process guidelines for magnetic TSAs that are outlined in the final section of the manuscript. The design guidelines are then used to design and fabricate a surgical tool prototype, and the gripping force, wireless actuation, and integration potential of the prototype are briefly discussed.

II. Analytical Model of the TSA

A. The Magnetically-Actuated TSA Concept

A magnetic twisted string actuator is shown conceptually in Fig. 1-(A) as two strings with a magnet attached at the center. To illustrate its application, the magnetic TSA is attached to a slider-crank mechanism that closes a surgical microforceps. Each string has an unstretched axial length L_0 and radial positions r_i. Rotation of the magnet by angle θ_0 results in a twist in the string, as shown in Fig. 1-(B). Assuming

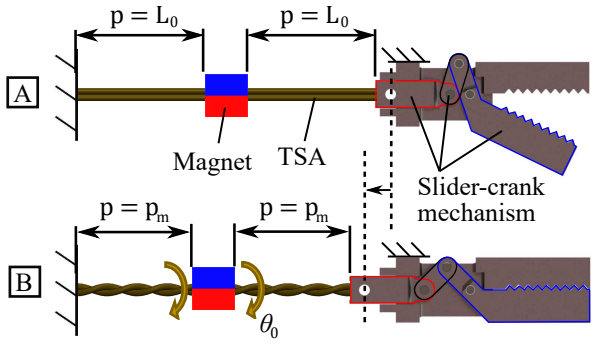

Fig. 1. Magnetic twisted string actuator (TSA) concept, actuating an example surgical gripper mechanism. (A) Initially the string is untwisted (string length p equals initial fiber length L_0) and the gripper is open. (B) As the magnet rotates, the string is twisted. If there is minimal load the fiber lengths L_0 remain constant, so the string length p shortens to the axial length of the outermost fibers p_m. As the string shortens, the gripper closes. If the gripper encounters a rigid object as it closes, the string length p becomes constant and a force is exerted on the object as the fibers elongate.

the gripper encounters minimal force as it closes, the fibers will maintain their original length L_0: the fiber arrangement changes to a helix while the axial length p of the string shortens, closing the gripper, as shown in Fig. 1-(B).

However, if the gripper encounters a rigid object or obstruction as it closes, the string length p will become fixed, as shown in Fig. 1-(B). As the string is twisted past the point of contact by an angle θ, the fibers in the string will undergo strain as the fiber helix twists further, shown in Fig. 2-(A). As described earlier by [25] and shown by the simplified string geometry in Fig. 2-(B), the strain in the fibers results in a force F along their length. The fibers form an angle φ with the string axis; therefore, the fiber tension force has an axial component F_z and a circumferetntial component F_r. The rotational input (in this case the magnet) needs to apply a torque τ_m to overcome the torque couple τ_s due to the circumferential force components of the fibers in the string and produce the desired output axial force.

The onboard magnet can be accurately modelled as a dipole due to the large distance between it and the external magnetic field source. The point dipole assumption provides a simple model to predict the resultant torque $\boldsymbol{\tau}_m$ on a magnetic dipole (magnet) $\boldsymbol{m}$ subjected to a magnetic field $\boldsymbol{b}$ (in tesla):

$$\tau_m = \|\boldsymbol{m}\|\|\boldsymbol{b}\| \sin(\gamma)\,, \tag{1}$$

where γ denotes the angle between the dipole vector and the field vector. The magnetic torque is maximized when the field vector and the dipole vector are perpendicular $\gamma = \pm 90°$and is equal to zero when they are parallel $\gamma = 0°$or $180°$. In the absence of other torques, the magnetic torque will drive γ to zero: the magnet will align itself to the field like a compass needle. As a result, a rotating magnetic flux density will cause the magnet to rotate with it. However, the TSA applies a resisting elastic torque τ_s that causes the magnet to lag behind the flux density vector by a phase lag γ such that $\tau_m + \tau_s \approx 0$. As the TSA is twisted further, the resisting torque increases

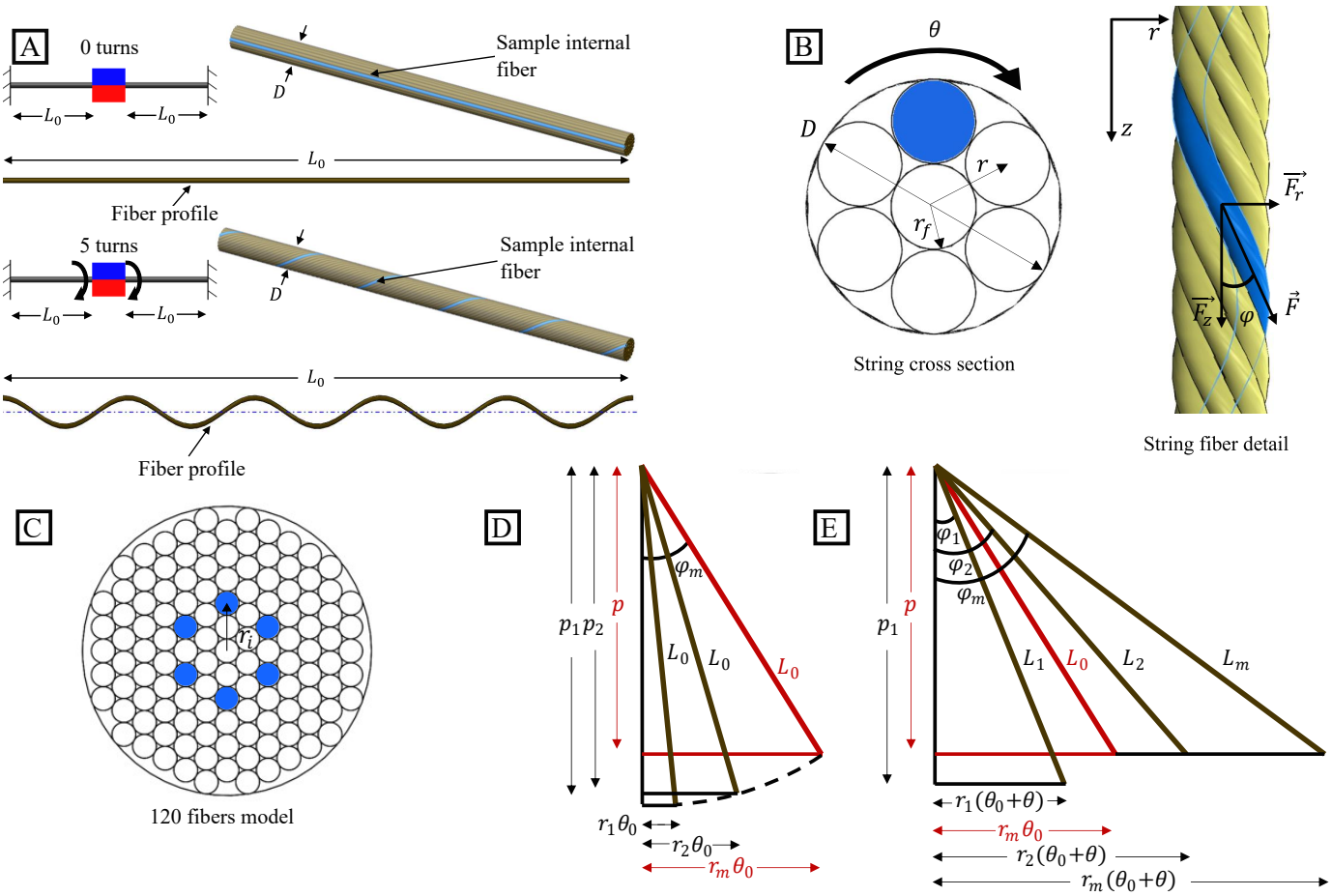

Fig. 2. Dynamic model of a TSA. (A) Fixed-displacement twisted string setup at 0 turns and 5 turns. (B) Geometrical representation of a 6 fiber twisted string. The strain in each fiber produces both an axial force and a resisting torque in the TSA due to the helix angle of each fiber φ_i. (C) 120 fiber cross section model. An example group of fibers that share a common radius r_i is highlighted in blue. (D) Diagram showing the fiber lengths under minimal load as the string is twisted until it reaches a blocking point after initial twist θ_0. Note that the lengths of fibers 1, 2, and m are equal to L_0, but their circumferential displacement from the top of the fiber to the bottom of the fiber $r\theta$ differ due to their radial distances (r_1, r_2, r_m) from the center of the string. As a result, after an initial twist θ_0, only the outermost fiber at r_m has reached an axial length of p (the blocked length). (E) Diagram showing the fiber lengths under fixed axial displacement p after the blocking point has been reached and after some additional twist θ after the initial twist θ_0. Now the outermost fiber at r_m has increased in length from its initial length L_0 to some final length L_m. However, the innermost fiber at r_1 has yet to reach the blocked length p; therefore $L_1 = L_0$ (no strain in that fiber), so the fiber is said to be "inactive" (it contributes no force).

until the phase lag between the magnet and the flux density exceeds 90°. At this point the magnetic torque will decrease and the TSA will slip back one or more turns. This slippage point is a critical difference between magnetic actuation for TSAs and conventional actuation methods like DC motors, which simply reach a stall torque and hold their position. It is therefore essential to characterize the TSA behavior so that the conditions that result in magnet slip can be avoided.

B. An Analytical Model for Predicting Magnetically Actuated TSA Force and Torque

The following discretized analytical model was developed to predict the TSA force generation. While the kinematics of the TSA was thoroughly covered by [26], the dynamics of the TSA was only briefly modelled by [25] for simple strings composed of six parallel fibers at a common radius from the central axis that undergo twisting under a spring-damper resistance. In this work, a more general model is derived, that assumes the string to be composed of many fibers arranged at multiple radii from the central axis. Additionally, the scenario where a string shortens through twisting until it reaches an axial blocking point, and subsequently generates an axial force through additional twisting, is analyzed for the first time.

As shown in Fig. 2-(C) it is assumed that a string is a cylinder composed of 120 discrete parallel fibers of circular cross section that have both longitudinal stiffness [26] and torsional stiffness. The fibers are grouped into m groups, where all the fibers of the i^{th} group share a common radial position r_i from the center of the string. Since the model only applies to the millimeter scale, gravitational forces are considered negligible. It is also assumed that all strains are within the elastic limit of the strings.

As illustrated conceptually in Fig. 2-(D), consider the case where a TSA is shortened initially after rotating by an angle θ_0 under negligible load until it reaches a blocking point. Further rotations, denoted by θ, do not shorten the string length p but instead purely contribute to an axial force buildup as the fibers elongate, as depicted in Fig. 2-(E). An example of this type of

movement is a TSA-actuated gripper grasping a rigid object.

Initially, the string is twisted under minimal load by an angle θ_0 as shown in Fig. 2-(D). All the fibers maintain a constant fiber length L_0 as the string is twisted. As a result, each group of fibers reaches a different shortened axial length of p_i after being twisted by a common angle θ_0 [25], determined by:

$$p_i = \sqrt{L_0^2 - (r_i\theta_0)^2}\,. \tag{2}$$

From (2), fiber groups with larger r_i experience more axial shortening; therefore, the initial twist θ_0 is defined as the twist required for the outermost fibers at $r_i = r_m$ to reach the blocked axial string length such that $p_m = p$, as shown in Fig. 2-(D) (rightmost triangle).

As the string is twisted by an angle θ past the initial twist θ_0, the inner fiber groups continue to shorten axially until they reach the blocked axial length p. After reaching an axial length of p, further twisting results in an elongation of the fibers in each group such that the fiber length L_i increases to

$$L_i = \sqrt{p^2 + \left(r_i\left(\theta + \theta_0\right)\right)^2}\,. \tag{3}$$

The strain in each fiber results in a corresponding stress or elastic force acting along the length of each fiber:

$$F_i = EA\left(L_i - L_0\right)/L_0 \tag{4}$$

where E is the Young's modulus of the fiber material and $A = \pi r_f^2$ is the cross-sectional area of an individual fiber. Due to the helix angle of each group of fibers φ_i, the force in each fiber can be split into a component acting along the axis of the string and a component that produces a torque about the string axis, as shown in Fig. 2-(B). The overall axial force F_z and required input torque τ_s for the TSA can then be determined from the summation of the individual contributions of each fiber group:

$$F_z = \sum_{i=1}^{m} n_i \frac{pEA(L_i - L_0)}{L_i L_0}\,, \tag{5}$$

$$\tau_s = \left(\sum_{i=1}^{m} n_i \frac{EAr_i^2(L_i - L_0)}{L_i L_0}\left(\theta + \theta_0\right)\right) + nGJ\frac{\theta + \theta_0}{L_0}\,, \tag{6}$$

where n_i is the number of fibers in the i^{th} group of fibers, n is the total number of fibers, G is the shear modulus of the fiber material, and J is the torsional constant of each fiber. In (6), the additional resisting torque developed due to the torsion of each individual fiber is accounted for in the second term based on beam torsion theory [30]. This torsional resisting torque of each fiber is multiplied by the total number of fibers in the model to determine the total torsional resisting torque of the string.

The magnetically actuated TSA has two separate strings: one on either side of the magnet. As a result, for a given twist of the magnet θ the torque on the magnet should be two times that predicted from (6). This analytical model enables a reasonable prediction of the TSA dynamics during twisting, but several simplifying assumptions were required to arrive at this result. Experimental validation is therefore critical to a successful TSA design.

C. TSA Dimensional Analysis

The Buckingham Pi theorem allows a phenomenon with known independent physical parameters to be re-written as a function of dimensionless parameters. The dimensionless parameters can then allow comparisons between conditions that are independent of scale and may also reduce the number of relevant variables when investigating the phenomenon. One of the best-known results of this method is the Reynolds number in fluid dynamics.

The model for the TSA axial force, equation (5), can be written as a function of five independent physical parameters:

$$F_z = f\left(E, D, L_0, \theta_0, \theta\right)\,, \tag{7}$$

This relationship can be made dimensionless by defining several Pi terms: $\Pi_1 = F_z/ED^2$ (the normalized force), $\Pi_2 = L_0/D$ (the characteristic length ratio or normalized string length), $\Pi_3 = \theta_0$, and $\Pi_4 = \theta$ such that

$$\Pi_1 = \phi\left(\Pi_2, \Pi_3, \Pi_4\right)\,. \tag{8}$$

As a result, the normalized force Π_1 will allow direct performance comparisons across TSAs with different material properties and across different scales. What should remain is the behavior of each TSA as a function only of its geometry.

III. Experimental Validation

A series of experiments were conducted to validate the analytical model and to characterize the behavior of the TSA.

A. Materials and Methods

1) Experimental Apparatus: An ATI Nano17T S-8-0.05 6-axis load cell was used to measure the axial force and resisting torque developed within the TSAs. The experimental apparatus depicted in Fig. 3-(A) and (B) was placed within a Helmholtz coil system that applied a rotating magnetic field with a flux density of 20 mT. All components were made of aluminum or brass to prevent magnetization that might affect the measurements. This magnetic field applied a magnetic torque to the magnets on the TSA, thereby twisting the strings.

2) String Preparation Procedure: One necessary step was to prepare the TSA prior to the experimental measurements. The preparation procedure consisted of twisting the TSA for 50 cycles, 3 consecutive times, while waiting 5 minutes between each twisting sequence. The preparation procedure was performed with a magnetic field strength of 20 mT rotating at 10 Hz for a number of turns greater than or equal to the desired testing number of turns plus one. For example, an experiment involving twisting a TSA by 10 turns would have a preparation procedure with 11 turns. This preparation was necessary to avoid a non-negligible elongation in the strings that occurs the first time they are twisted. This behavior has also been observed by other authors [26], who used a similar preparation procedure.

Even after the TSA preparation procedure, there would be negligible force buildup during the first several turns. It was observed that the strings would assemble themselves from a

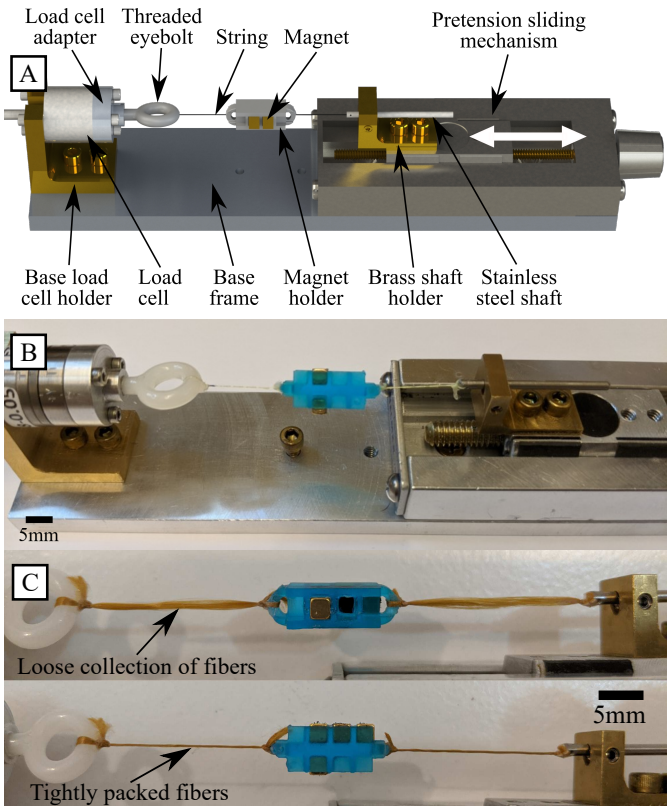

Fig. 3. Experimental apparatus for measuring TSA force and torque. (A) CAD model with labeled components. (B) Photograph of the apparatus. (C) Initial pretwisting by an angle of θ_0 before reaching the axial force build-up stage.

loose collection of fibers into a tight helix after these first few turns, as shown in Fig. 3-(C). As a result, even in the case when $p = L_0$, there would be an initial twist and therefore an initial helix angle. To minimize these ineffective initial turns, a sliding mechanism was used to ensure that the strings were relatively taut and straight before each set of measurements. A completely loose string would require a much larger number of turns to reach the initial string state described by the analytical model. However, a taut string would still have a loose collection of fibers when under zero twist. To account for this starting loose collection of fibers, the measured force curves were post-processed by choosing $\theta = 0$ to be the point where the axial force was equal to 1% of the maximum measured force for that experiment. At this point the fibers were observed to be tightly packed. Any preceding twist would be considered part of the initial twist θ_0, thereby accounting for the helix angle due to this initial twist. The 1% threshold was chosen because it was the most consistent method of determining the start of the force buildup, and such a small difference in the starting point of $\theta = 0$ did not significantly affect the model accuracy. It was also the value at which the uncertainty was approaching the noise level due to the string's vibration. Other methods of determining an axial force buildup were attempted, such as detecting a significant change in slope of the force curve, but the signal's noise made these results inconsistent.

TABLE I
STRING PROPERTIES.

String Material	Diameter (mm)	Young's Modulus E (GPa)	Reported Shear Modulus G (GPa)
Dyneema (B)	0.197	28.28	3 [31]
Dyneema	0.115	40.01	3 [31]
UHMWPE	0.088	47.52	3 [31]
Zylon	0.295	78.99	30.38 [32]
Kevlar	0.140	63.96	16.2 [33]
Nylon	0.238	2.82	4.1 [34]

3) String Material Properties: Previous work on twisted string kinematics has shown that braided and non-braided strings each have their advantages and disadvantages [26]. Braided strings tend to be more robust as well as easier to use, install and maintain. On the other hand, non-braided strings typically behave in a more predictable manner when shortening and allow for more precise control. We therefore used both types of strings in our experiments to determine which is preferable for force transmission, reliability, and accuracy.

We selected the following string materials:

- A Hercules 4 Strands Braided Fishing Line, made of a proprietary ultra-high-molecular-weight polyethylene (UHMWPE) material from DSM, which is often branded as Dyneema (referred to with the label "Braided Dyneema"),
- A non-braided Dyneema string material from the same supplier (referred to with the label "Dyneema"),
- A UHMWPE string from Fiberline (referred to with the label "UHMWPE"),
- A PBO (poly(p-phenylene-2,6-benzobisoxazole)) string often branded as Zylon (Toyobo) from Fiberline,
- A Kevlar string from Fiberline, and
- An Orvis Superstrong Plus Tippet, made of Nylon.

Though the Nylon string used in these experiments was a monolithic strand (i.e. not composed of multiple fibers) it was nevertheless modeled as a bundle of parallel cylindrical elements according to the previously stated assumptions.

The diameters of the strings were measured in several places using a micrometer and the averages of those measurements are shown in Table I. The measured string diameters were effectively the same as the diameters reported by the manufacturers of the string materials. The material properties of commercially available strings are often unreported, so it was necessary to measure the Young's modulus directly. The Young's moduli E of the string materials selected for the TSA were determined using an Instron Microtester 5848, with the results shown in Table I. The shear moduli of the materials reported by the manufacturer are also listed in Table I.

B. Results and Discussion

In our experiments, all string materials exhibited similar behaviors; therefore, for brevity, only the results for the ultra

high molecular weight polyethylene (UHMWPE) string are shown in Fig. 4 because it is the material that was chosen for the surgical tool prototype in Section IV. As explained in more detail in this section, the UHMWPE material was chosen due to its superiority compared to other materials tested in terms of durability and robustness, exhibiting the least fiber tearing after being subjected to fast twisting at a high number of turns. Additionally, the UHMWPE string was the thinnest string available, offering an innate advantage because it can achieve a higher peak axial force for a given available torque if the angle of pretwist is large (which is the case in the gripper application). The results for other materials can be found in the attached Supplementary Materials.

1) Predicted Force vs. Number of Turns: Fig. 4-(A) shows the experimental and predicted normalized force Π_1 as a function of the number of turns $\theta/2\pi$. The two parameters that change the shape of the Π_1 vs. θ curves are the characteristic length ratio $\Pi_2 = L_0/D$ of the string and the amount of initial twist θ_0. The dotted lines in Fig. 4-(A) show the predicted effect of different values of θ_0 on the normalized force Π_1 based on the analytical model for a characteristic length ratio of $\Pi_2 = 171$.

The theoretical normalized force in Fig. 4-(A) from the analytical model (5) (dotted line), slightly under-predicts the measured experimental normalized force (solid line). The overall behavior of the normalized force as a function of the number of turns is well captured in this specific case, with an error of less than 10%. A full breakdown of the force results for multiple string materials and geometries can be found in the Supplementary Material (Table S2) with some additional sample plots for different string materials (Fig. S2). Most of the cases tested had length ratios in the range of $100 < L/D < 200$, so it cannot be concluded whether the analytical model is effective outside of those ranges. The model was found to be able to predict the peak output force of the TSA for a given θ to within $\pm 20\%$ for a variety of string materials and characteristic length ratios. This level of accuracy is useful for informing choices in the design of TSA devices by pointing to good solutions, but iteration of the design process over multiple TSA prototypes with experimental validation remains necessary to refine designs and to precisely satisfy force requirements.

Some sources of error that explain the slight discrepancy between the theoretical and experimental axial force results are that the string cross section might not be perfectly circular as assumed in the derivation, the fibers are not perfectly parallel and are tangled in some portions of the string, the number of fibers is estimated and is difficult to determine accurately, most likely requiring microscopy techniques, the number of fibers changes along the length of the string, due to the unavoidable nature of the string manufacturing process, and finally, the fibers tear with many cycles of twisting/untwisting. Additionally, the torque absolute values were shown to be consistently and significantly under predicted by (6), which is a focus point of future work. The results presented here indicate that experimental validation of TSA designs is especially critical for determining the required input torque. Otherwise, the use of a safety factor of 4-13 would be needed.

2) Viscoelastic Behavior: Viscoelastic behavior is a well-known challenge in modeling TSAs [35]. All TSAs showed hysteresis in their axial force twisting/untwisting cycles, which can be seen in Fig. 4-(B) (see also Fig. S3). Hysteresis was also present in the measured torque, which can be found in the Supplementary Materials (Fig. S8). The force on the untwisting cycle was lower than the force on the twisting cycle. This behavior is not captured by the model and may be due to inter-fiber friction effects. Other authors have developed phenomenological models to account for hysteresis effects in TSA kinematics [28], so it is possible that similar methods could be applied in the future to improve the accuracy of the model for the axial force of the TSA.

All strings exhibited stress relaxation over a short period of roughly 30 seconds, which can be seen in Fig. 4-(D) (see also Fig. S5). The TSA was twisted 7 turns and then held at a constant angle for around 30 seconds. The axial force decreases from the peak value quickly, then appears to reach a constant value. However, polyethylene strings, namely the UHMWPE and braided Dyneema strings, exhibited much more stress relaxation than other types of fibers (Zylon, Kevlar). The decrease in force over 30 seconds was 50.3% for the braided Dyneema, 39.3% for UHMWPE, 26.8% for Kevlar and 22.4% for Zylon. We can therefore conclude that Zylon and Kevlar are preferable for applications that require precise control of static forces over long time periods.

The TSA exhibited fatigue behavior, which is illustrated in Fig. 4-(C). The TSA was twisted and untwisted by 8 turns over 100 cycles. There is a reduction in peak force between cycles that is most prominent in the first 10-20 cycles. From there the maximum output force appears to level off. We observed that UHMWPE exhibited more fatigue than Kevlar (see Fig. S4), with a reduction of 26.5% and 20.3% respectively, over 100 cycles. This unwanted behavior is likely due to plastic deformation of the strings, especially the outermost fibers which experience the largest strains. In fact, we observed visually that some outer fibers were torn after performing 100 loading cycles. Strings that exhibited more stress relaxation (such as UHMWPE and Dyneema) tended to show less of this tearing. Therefore, for applications that require frequent twisting at high speeds, care must be taken to calculate the minimum acceptable axial force and choose a string that can be twisted a higher number of turns without breaking. UHMWPE is superior with respect to these considerations.

Considering these viscoelastic behaviors of the TSA (hysteresis, fatigue, stress relaxation), it was necessary to check for rate dependent stress. Two different UHMWPE strings were twisted to $\theta/2\pi = 12$ turns at a series of rotation frequencies from 1 Hz to 39 Hz and their peak force was measured. The results of these tests are shown in Fig. 4-(E). Despite the other viscoelastic behaviors of the TSA, the peak force did not appear to show any significant rate dependence over the selected range of frequencies.

The following conclusions can be drawn regarding the design tradeoffs of TSAs, and they hold well for small pretwisting angles. 1) For all other parameters remaining constant, increasing the string length has no effect on the torque required to achieve a given force. However, the total

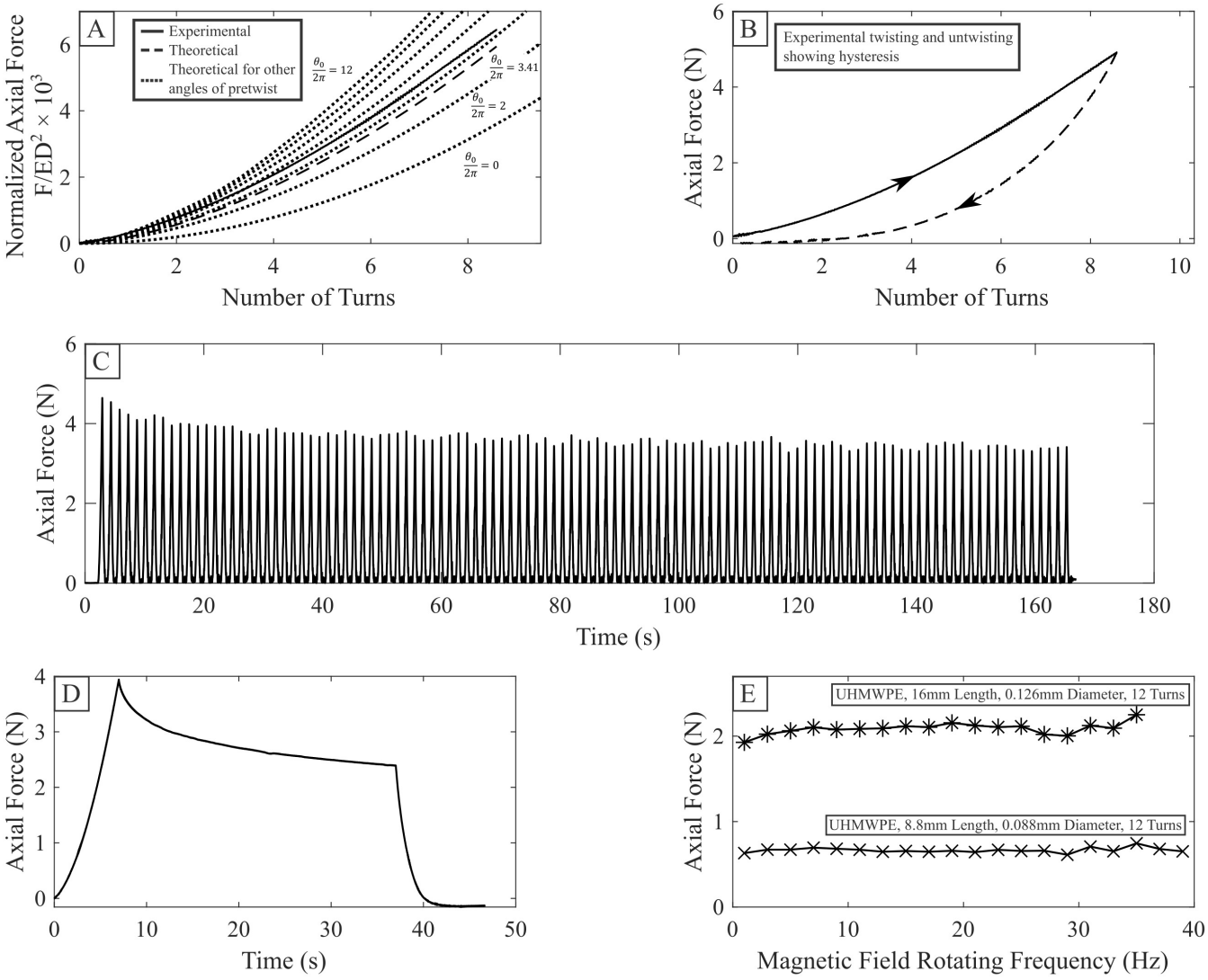

Fig. 4. Characterization results for ultra-high molecular weight polyethylene (UHMWPE) string. (A) Normalized axial force vs number of turns ($\Pi_2 = 171$). (B) Hysteresis in axial forceafter twisting (solid) and untwisting (dashed) past the blocking point ($\theta_0/2\pi = 3.41$). (C) Fatigue behavior in axial force after 100 twist-untwist cycles (each cycle consisted of 8 turns). (D) Stress relaxation behavior after twisting 7 turns, holding for 30 seconds and untwisting. (E) Rate dependence of maximum output force after 12 turns.

number of turns required increases and the string will be prone to failure. 2) For all other parameters remaining constant, increasing the string diameter will reduce the torque required to achieve a given force. However, the achievable force will rapidly decrease with increasing angles of initial twist. 3) For all other parameters remaining constant, choosing a string with a larger Young Modulus will reduce the torque required to achieve a given force. However, the achievable force will rapidly decrease with increasing angles of initial twist.

IV. Design of a Magnetically-Actuated TSA

A. TSA Design Process Guidelines

In the light of the conclusions drawn from the experimental validation, the following process can be followed to design a magnetic TSA for a particular application. 1) Determine the target axial force including a safety factor of perhaps 20%, to account for the mathematical model uncertainty, as described in the previous sections. 2) Select the string material. As shown previously, UHMWPE is superior in terms of robustness and durability, while Kevlar and Zylon are preferred for precise control and minimal viscoelasticity. 3) Select the L/D ratio, depending on the physical space available. Thinner strings are preferred, because they provide a higher transmission gearing ratio than bulkier strings for a given number of turns. However, thinner strings are prone to early failure. The L/D ratio should ideally be between 100 and 200 for best model performance. 4) Determine the total number of turns needed to achieve a desired stroke length. 5) Determine the required torque to achieve a desired axial mechanism force.

B. Gripper Prototype

To demonstrate the performance of a magnetic TSA in a practical application, a surgical gripper prototype was designed and manufactured with a magnetic TSA that can fit through a 3

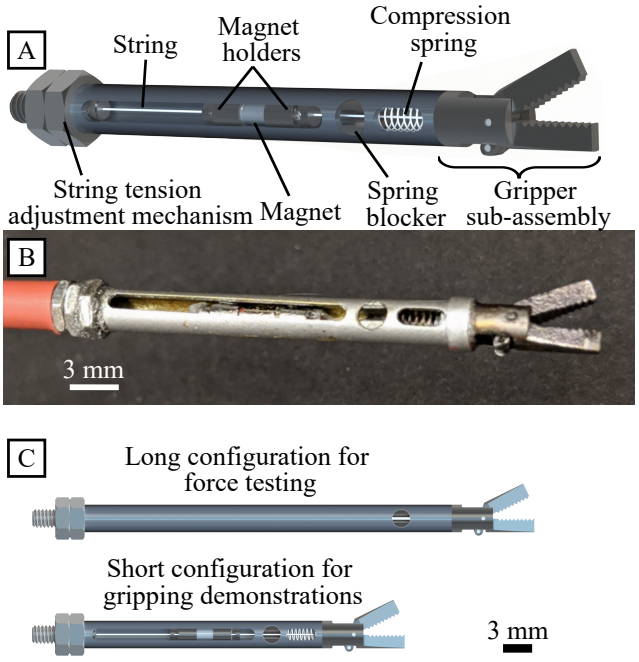

Fig. 5. Magnetic twisted string surgical tool design concept. (A) CAD model with labeled gripper and TSA components. (B) Photograph of the final gripper design. (C) CAD illustrations of long and short configurations of the surgical tool.

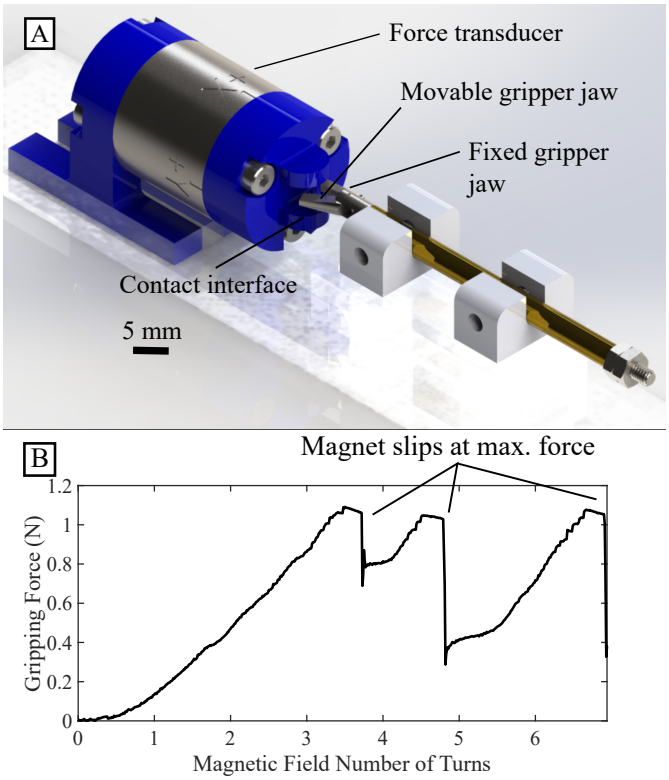

Fig. 6. Gripping force experimentally measured for a constantly rotating input magnetic field for the long gripper design. (A) The experimental setup used to measure the gripping force with an ATI Nano17T force sensor. (B) Plot of the gripping force versus number of turns. The magnet rotates until the slippage point, shown by the drops in force. Subsequently, the magnet re-synchronizes with the field and the force begins increasing until the slippage point is reached again.

mm diameter endoscopic port. The gripper is shown in Fig. 5. The TSA, enclosed in brass tubing for protection, is used to actuate the movable gripper jaw while the other jaw stays fixed. When a rotating magnetic field is applied around the tool long axis, the magnet rotates and twists the string, closing the gripper. A compression spring provides a restoring force to return the gripper to its normally-open state when the string is untwisted. Two magnetic TSA gripper design configurations were tested: a long configuration to test for maximum force and tissue retraction and a short configuration to demonstrate untethered operation and closure speed capabilities, as shown in Fig. 5-(C).

The achievable gripping force of the surgical tool was measured using the apparatus in Fig. 6-(A). The moving gripper jaw was secured in a resin jig that was fitted to the 6 axis load cell and a 20 mT rotating magnetic field was applied, at 5 Hz, to rotate the magnet until the string resisting torque overpowers the applied magnetic torque causing the twisted string actuator to ”slip” back several turns. The vector sum of the forces in all 3 axes of the load cell was measured as a function of time. The resulting force is shown in Fig. 6-(B), with a peak gripping force of 1.09 N. It is a factor of 62 increase from previous magnetic microsurgical grippers which only achieve 18 mN of force for the same actuating magnetic field [6]. An alternative comparison is the output force per unit input torque for the magnetic TSA gripper compared to the gripper in [5]. The mechanical advantage of the gripper in [5] was approximately 0.18 N/N·mm whereas the magnetic TSA gripper had a mechanical advantage of 6.23 N/N·mm: a factor of 35 increase. Another comparison could be made, where the comparing factor is the tool’s total volume. The previous design occupies a space of approximately 42 mm^2, which the TSA surgical tools has a volume of 420 mm^2. Therefore, the previous design’s force per unit volume results in 0.418 N/mm^2, while the current design’s value is 2.59 N/mm^2, a factor of 6.2 increase. This indicates that further miniaturizing the TSA surgical tool should be a priority, because it maintains a clear mechanical advantage across all comparative methods.

The capability of the gripper to retract and tear tissue was demonstrated in Fig. 7. Raw chicken breast tissue at room temperature was used as a tissue analog. A 20 mT magnetic field rotating at 5 Hz for 12 turns was used to close the gripper jaws on the tissue. The magnetic field was then held at a constant angle as the gripper was pulled manually to retract the tissue.

C. Integration with Other Robotic Components

To demonstrate its potential for integration into a surgical robotic system, the magnetic TSA gripper was attached to the end of a 2 mm diameter continuum tube robot (CTR) arm, as shown in Fig. 8-(A).

The gripper can be actuated within an electromagnetic coil system, as shown in Fig. 8-(B), or by the field of a nearby rotating permanent magnet (see the Supplementary Video). The surgical tool can be operated as a standalone assembly

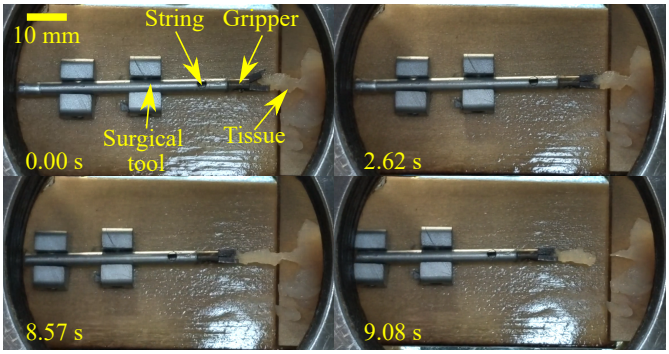

Fig. 7. Tissue gripping test. Inside the Helmholtz coil system, a 20 mT magnetic field rotating at 5 Hz was applied for 12 turns, closing the gripper on the tissue. The field angle was then held constant (no rotation) to hold the gripper closed as the tool was pulled away from the tissue, tearing off a small piece.

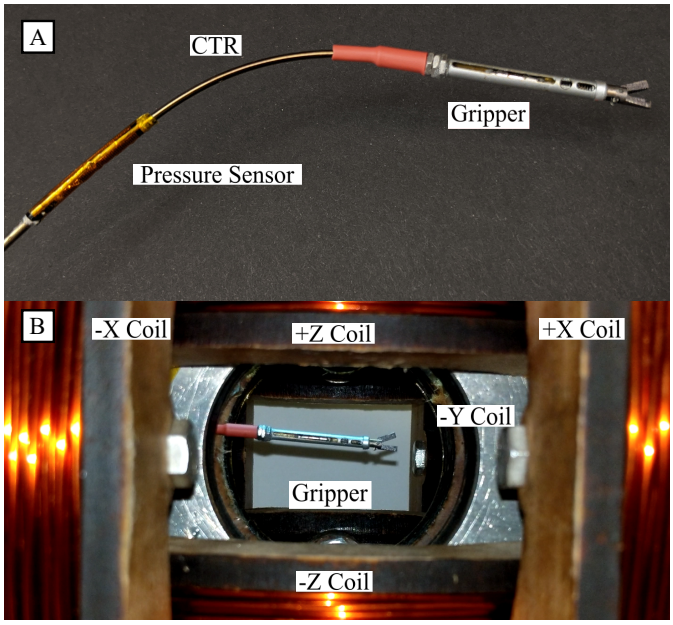

Fig. 8. Gripper integrated with a continuum tube robot (CTR). (A) The gripper is mounted at the end of a continuum tube robot with a pressure sensor on the robot to sense contact with surrounding tissue. (B) Gripper inside of the 3-axis Helmholtz electromagnetic coils (See the supplementary video).

without any exterior connection, which was demonstrated by placing it on a table and generating a small rotating magnetic field by spinning a permanent magnet nearby with a simple power drill. The closure speed of the gripper was measured by actuating it with a 20 mT magnetic field rotating at 40 Hz in the Helmholtz coil system. Though the TSA is designed to produce low-speed, high-torque outputs, the gripper jaws can be closed relatively quickly in less than 0.4 seconds. This shows that the gripper can potentially be utilized for surgical applications where closure speed is important, such as quickly cutting or pinching tissue.

From the results shown, we conclude that using a magnetic TSA is a feasible option for actuating a microsurgical forceps if it is combined with a system that can produce magnetic fields over a relatively large patient workspace, such as the one presented in [23]. Additionally, we demonstrated that the magnetic TSA surgical gripper is untethered, and it can be operated as a standalone unit with potential for MIS.

V. Limitations and Future Work

Due to its limited accuracy, it is unlikely that this analytical model can be used for control methods beyond the most basic open loop control demonstrated in this study (to open/close the gripper and apply increasing or decreasing force). Predicting the input torque accurately and accounting for force hysteresis remains an important area of future investigation to ensure the effectiveness and safety of TSAs for medical applications. A recent study has shown that TSAs can be designed with self-sensing properties to predict their length [28], which may be an avenue for more precise control of miniature magnetic TSAs. However, such a measurement system would require a tether for sensor signal lines and necessitates the use of conductive string materials.

Further miniaturization of the transmission, especially in the axial direction, would result in a more compact tool. The strength of the tool could be increased by increasing the amount of magnetic material, which could possibly surround the strings for the length of the transmission. The speed of the transmission is sometimes limited by vibrations which occur due to the weight of the suspended magnet. These vibrations could be reduced by constraining the magnet in the radial direction. The tendency of the mechanism to slip near the critical tension point could be alleviated by adding a ratcheting mechanism to prevent back-slip. Finally, high tensile strength biocompatible string materials, that can withstand large strain, must be explored for medical use.

Acknowledgment

The authors would like to thank Thomas Looi, Jim Drake, and Hani Naguib for their advice and ideas on framing the surgical tool design, testing, demonstration, and future applications. We would also like to thank Jongwoo Kim and Tianhao Chen for their time and expertise helping to integrate of the magnetic tool with the robot and measure the material properties of the strings, respectively.

References

[1] J. J. Abbott, E. Diller, and A. Petruska, "Octomag: An electromagnetic system for 5-dof wireless micromanipulation," *Annu. Rev. Control Robot. Autonomous Syst*, vol. 3, no. 6, pp. 57–90, 2020.

[2] B. J. Nelson, I. K. Kaliakatsos, and J. J. Abbott, "Microrobots for minimally invasive medicine," *Annu. Rev. Biomed. Eng.*, vol. 12, no. 1, pp. 55–85, 2010.

[3] H. J. Marcus, A. Hughes-Hallett, T. P. Cundy, G.-Z. Yang, A. Darzi, and D. Nandi, "da Vinci robot-assisted keyhole neurosurgery: a cadaver study on feasibility and safety," *Neurosurg. Rev.*, vol. 38, no. 2, pp. 367–371, Apr. 2015.

[4] H. J. Marcus, K. Zareinia, L. S. Gan, F. W. Yang, S. Lama, G.-Z. Yang, and G. R. Sutherland, "Forces exerted during microneurosurgery: a cadaver study," *Int. J. Med. Robot. Comput. Assist. Surg.*, vol. 10, no. 2, pp. 251–256, 2014.

[5] A. Lim, A. Schonewille, C. Forbrigger, T. Looi, J. Drake, and E. Diller, "Design and comparison of magnetically-actuated dexterous forceps instruments for neuroendoscopy," *IEEE Trans. Biomed. Eng.*, vol. 68, no. 3, pp. 846–856, 2021.

[6] C. Forbrigger, A. Lim, O. Onaizah, S. Salmanipour, T. Looi, J. M. Drake, and E. Diller, "Cable-less, Magnetically-Driven Forceps For Minimally Invasive Surgery," *IEEE Robot. Autom. Lett.*, vol. 4, no. 2, pp. 1202–1207, Apr. 2019.

[7] O. Onaizah and E. Diller, "Tetherless mobile micro-surgical scissors using magnetic actuation," in *IEEE International Conference on Robotics and Automation*, Montréal, Canada, May 2019, pp. 894–899.

[8] M. P. Kummer, J. J. Abbott, B. E. Kratochvil, R. Borer, A. Sengul, and B. J. Nelson, "Octomag: An electromagnetic system for 5-dof wireless micromanipulation," *IEEE Trans. Robot.*, vol. 26, no. 6, pp. 1006–1017, 2010.

[9] L. Feng, X. Wu, Y. Jiang, D. Zhang, and F. Arai, "Manipulating microrobots using balanced magnetic and buoyancy forces," *Micromachines*, vol. 9, no. 2, p. 50, 2018.

[10] S. Martel and M. Mohammadi, "Using a swarm of self-propelled natural microrobots in the form of flagellated bacteria to perform complex micro-assembly tasks," in *IEEE International Conference on Robotics and Automation*, 2010, pp. 500–505.

[11] Q. Fu, S. Guo, S. Zhang, H. Hirata, and H. Ishihara, "Characteristic evaluation of a shrouded propeller mechanism for a magnetic actuated microrobot," *Micromachines*, vol. 6, pp. 1272–1288, Sept. 2015.

[12] E. Diller, J. Giltinan, P. Jena, and M. Sitti, "Three dimensional independent control of multiple magnetic microrobots," in *IEEE International Conference on Robotics and Automation*, Karlsruhe, Germany, May 2013, pp. 2576–2581.

[13] S. Jeong, H. Choi, K. Cha, J. Li, J.-O. Park, and S. Park, "Enhanced locomotive and drilling microrobot using precessional and gradient magnetic field," *Sens. Actuators A: Phys.*, vol. 171, no. 2, pp. 429 – 435, 2011.

[14] X. Tang, D. Zhang, Z. Li, and J. Chen, "An omni-directional wall-climbing microrobot with magnetic wheels directly integrated with electromagnetic micromotors," *Int. J. Adv. Robot. Syst.*, vol. 9, p. 16, 2012.

[15] B. R. Donald, C. G. Levey, C. D. McGray, D. Rus, and M. Sinclair, "Power delivery and locomotion of untethered microactuators," *Journal of Microelectromechanical Systems*, vol. 12, no. 6, pp. 947–959, 2003.

[16] H. McClintock, F. Temel, N. Doshi, J.-S. Koh, and R. Wood, "The millidelta: A high-bandwidth, high-precision, millimeter-scale delta robot," *Science Robotics*, vol. 3, p. eaar3018, Jan. 2018.

[17] F. A. Lavergne, H. Wendehenne, T. Bäuerle, and C. Bechinger, "Group formation and cohesion of active particles with visual perception–dependent motility," *Science*, vol. 364, no. 6435, pp. 70–74, 2019. [Online]. Available: https://science.sciencemag.org/content/364/6435/70

[18] S. Palagi, D. P. Singh, and P. Fischer, "Light-controlled micromotors and soft microrobots," *Advanced Optical Materials*, vol. 7, no. 16, p. 1900370, 2019.

[19] F. Guo, Z. Mao, Y. Chen, Z. Xie, J. P. Lata, P. Li, L. Ren, J. Liu, J. Yang, M. Dao, S. Suresh, and T. J. Huang, "Three-dimensional manipulation of single cells using surface acoustic waves," *Proceedings of the National Academy of Sciences*, vol. 113, no. 6, pp. 1522–1527, 2016.

[20] A. Marzo, S. Seah, B. Drinkwater, D. Sahoo, B. Long, and S. Subramanian, "Holographic acoustic elements for manipulation of levitated objects," *Nature communications*, vol. 6, p. 8661, 10 2015.

[21] F. Soto, A. Martin, S. Ibsen, M. Vaidyanathan, V. Garcia-Gradilla, Y. Levin, A. Escarpa, S. C. Esener, and J. Wang, "Acoustic microcannons: Toward advanced microballistics," *ACS Nano*, vol. 10, no. 1, pp. 1522–1528, 2016, pMID: 26691444. [Online]. Available: https://doi.org/10.1021/acsnano.5b07080

[22] E. Y. Erdem, Y. Chen, M. Mohebbi, J. W. Suh, G. T. A. Kovacs, R. B. Darling, and K. F. Böhringer, "Thermally actuated omnidirectional walking microrobot," *Journal of Microelectromechanical Systems*, vol. 19, no. 3, pp. 433–442, 2010.

[23] J. Rahmer, C. Stehning, and B. Gleich, "Remote magnetic actuation using a clinical scale system," *PLoS ONE*, vol. 13, no. 3, pp. e0 193 546(1–19), 2018.

[24] K. Fu, A. Knobloch, F. C. Martinez, D. C. Walther, C. Fernandez-Pello, P. Pisano, and D. Liepmann, "Design and fabrication of a silicon-based MEMS rotary engine," in *Proceedings of the ASME International Mechanical Engineering Congress and Exposition*, New York, USA, Nov. 2001.

[25] G. Palli, C. Natale, C. May, C. Melchiorri, and T. Wurtz, "Modeling and control of the twisted string actuation system," *IEEE/ASME Trans. Mechatron.*, vol. 18, no. 2, pp. 664–673, 2013.

[26] I. Gaponov, D. Popov, and J.-H. Ryu, "Twisted string actuation systems: A study of the mathematical model and a comparison of twisted strings," *IEEE/ASME Trans. Mechatron.*, vol. 19, pp. 1–12, 08 2014.

[27] T. Würtz, C. May, B. Holz, C. Natale, G. Palli, and C. Melchiorri, "The twisted string actuation system: Modeling and control," in *IEEE/ASME International Conference on Advanced Intelligent Mechatronics*, July 2010, pp. 1215 – 1220.

[28] D. Bombara, R. Konda, and J. Zhang, "Experimental characterization and modeling of the self-sensing property in compliant twisted string actuators," *IEEE Robotics and Automation Letters*, vol. 6, no. 2, pp. 974–981, 2021.

[29] B. Suthar, M. Usman, H. Seong, I. Gaponov, and J. Ryu, "Preliminary study of twisted string actuation through a conduit toward soft and wearable actuation," in *IEEE International Conference on Robotics and Automation*, Brisbane, Australia, May 2018, pp. 2260–2265.

[30] R. C. Juvinall and K. M. Marshek, *Fundamentals of Machine Component Design*. Wiley, 2012.

[31] "Ultra high molecular weight polyethylene fiber from dsm dyneema," https://www.gruschwitz.com/en/, accessed: May 2020.

[32] "Toyobo zylon® hm fiber/epoxy matrix unidirectional composite," http://www.matweb.com/search/datasheet.aspx?matguid=1a5f4985c8fb449da6edaec7813acf70, accessed: May 2020.

[33] C.-L. Tsai and M. Daniel, "Determination of shear modulus of single fibers," *Exp. Mech.*, vol. 39, pp. 284–286, Dec. 1999.

[34] Engineering Toolbox, "Modulus of rigidity," https://www.engineeringtoolbox.com/modulus-rigidity-d_946.html, 2005, accessed: May 2020.

[35] J. Zhang, J. Sheng, C. T. O'Neill, C. J. Walsh, R. J. Wood, J. H. Ryu, J. P. Desai, and M. C. Yip, "Robotic Artificial Muscles: Current Progress and Future Perspectives," *IEEE Trans. Robot.*, vol. 35, no. 3, pp. 761–781, 2019.

Mihai Nica received his Bachelor of Engineering in Mechanical Engineering in 2017 from Concordia University in Montréal, Canada. He worked from 2017 to 2018 as a mechanical designer at Elekta, a Swedish radiotherapy company. From 2018 to 2020, he completed his Master of Applied Science (MASc) at the University of Toronto, in the Microrobotics Laboratory, with particular interest in the field of minimally invasive medical tools and robots. In 2020, he started his medical degree (M.D.) at the University of Sherbrooke.

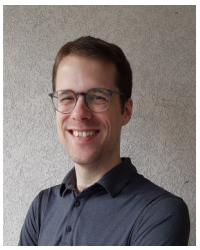

Cameron Forbrigger received his B.Eng. in 2015 and his M.A.Sc. in 2017 from Dalhousie University in Halifax, Canada. He is currently a Ph.D. student in the Microrobotics Lab at the University of Toronto. His research interests include magnetic microrobots and miniature robots for surgical applications.

Eric Diller received the B.S. and M.S. degree in mechanical engineering from Case Western Reserve University in 2010 and the Ph.D. degree in mechanical engineering from Carnegie Mellon University in 2013. He is currently Associate Professor and Dean's Catalyst Professor in the Department of Mechanical and Industrial Engineering at the University of Toronto, where he is director of the Microrobotics Laboratory. His research interests include micro-scale robotics, and features fabrication and control relating to remote actuation of micro-scale devices using magnetic fields, micro-scale robotic manipulation, smart materials. He is an Associate Editor of the Journal of Micro-Bio Robotics and received the award for Best Associate Editor at the 2015 IEEE International Conference on Automation and Robotics, as well as the IEEE Robotics & Automation Society 2020 Early Career Award. He has also received the 2018 Ontario Early Researcher Award, the University of Toronto 2017 Connaught New Researcher Award, and the Canadian Society of Mechanical Engineering's 2018 I.W. Smith Award for research contributions in medical Microrobotics.